ATLAS CONF Note

ATLAS-CONF-2018-035

11th July 2018

Measurement of the $Z\gamma \to \nu\bar{\nu}\gamma$ Production Cross Section in pp Collisions at $\sqrt{s}$ =13 TeV with the ATLAS Detector and Limits on Anomalous Triple Gauge Couplings

The ATLAS Collaboration

The production of Z bosons in association with a high energy photon ($Z\gamma$ production) is studied in the neutrino decay channel of the Z boson using pp collisions at $\sqrt{s}$ = 13 TeV. The analysis uses a data sample with an integrated luminosity of 36.1 fb^{-1} collected by the ATLAS detector in 2015 and 2016. $Z\gamma$ events with invisible decays of the Z boson are selected by requiring significant missing transverse energy ($E_{\mathrm{T}}^{\mathrm{miss}}$) in conjunction with a single isolated photon with large transverse energy (E_{T}). The rate of $Z\gamma$ production is measured as a function of photon E_{T}, $E_{\mathrm{T}}^{\mathrm{miss}}$ and jet multiplicity. Evidence for anomalous triple gauge coupling is sought in $Z\gamma$ production with photon E_{T} greater than 600 GeV. No excess is observed relative to the Standard Model expectation, and upper limits are set on the strength of $ZZ\gamma$ and $Z\gamma\gamma$ couplings.

ATLAS-CONF-2018-035
11 July 2018

1 Introduction

The production of Z bosons in association with photons in proton–proton (pp) collisions has been studied at the Large Hadron Collider (LHC) since the beginning of its operation in 2010 [1–4]. These studies have been used to test the electroweak sector of the Standard Model (SM) and to search for new physics effects, such as the potential couplings of Z bosons to photons. As in previous publications from experiments at LEP [5–8] and the Tevatron [9–11], no experimental evidence has been found for anomalous properties of neutral bosons at the LHC. A new set of data from the second period of LHC operation opens frontiers for more accurate measurements of the di-boson production rate in pp collisions, and facilitates tests of triple gauge-boson couplings (TGCs) with higher precision.

This paper presents a measurement of $Z\gamma$ production with Z decay to neutrinos. The analysis uses 36.1 fb^{-1} of pp collisions data collected with the ATLAS detector[1] at the LHC, operating at a centre-of-mass energy of 13 TeV. The measurements are made both with no restriction on the recoil system X (inclusive events) and by requiring that the system X has no jets with $|\eta| < 4.5$ and $p_{\mathrm{T}} > 50$ GeV (exclusive events).

The $\nu\bar{\nu}\gamma$ final state in the SM can be produced by a Z boson decaying into neutrinos in association with photon emission from initial state quarks or quark/gluon fragmentation into photons. These processes are illustrated by the leading-order Feynman diagrams shown in Figure 1. An example of an anomalous triple gauge-boson coupling (aTGC) of Z bosons and photons is shown in Figure 1(d). Such couplings are forbidden at tree level in the SM, but can arise in theories that extend the SM [12, 13].

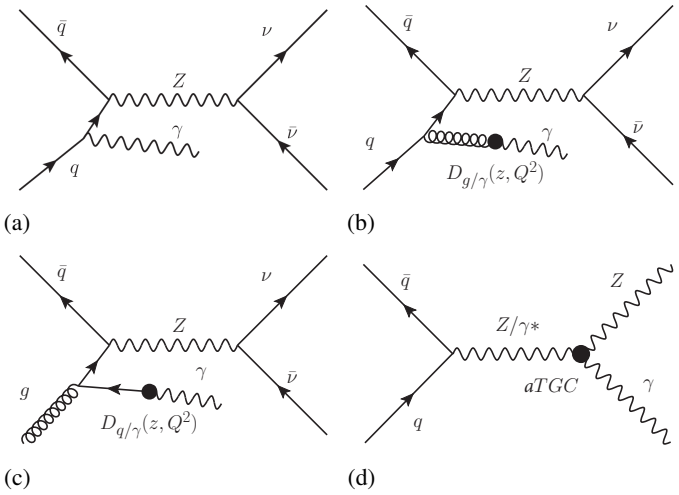

Figure 1: Feynman diagrams of $Z(\nu\bar{\nu})\gamma$ production: (a) initial-state photon radiation (ISR); (b,c) contributions from the $Z + q(g)$ processes when a photon emerges from the fragmentation of a quark or a gluon; and (d) aTGC vertex.

A study of the $Z(\nu\bar{\nu})\gamma$ process has several advantages over processes with Z decay to hadrons or charged leptons. The channel with hadrons in the final state is contaminated by a large multijet background. A

[1] ATLAS uses a right-handed coordinate system with its origin at the nominal interaction point (IP) in the centre of the detector and the z-axis along the beam pipe. The x-axis points from the IP to the centre of the LHC ring, and the y-axis points upward. Cylindrical coordinates (r, ϕ) are used in the transverse plane, ϕ being the azimuthal angle around the z-axis. The pseudorapidity is defined in terms of the polar angle θ as $\eta = -\ln\tan(\theta/2)$. Angular distance is measured in units of $\Delta R \equiv \sqrt{(\Delta\eta)^2 + (\Delta\phi)^2}$.

higher Z boson branching ratio into neutrinos relative to that into charged leptons provides an opportunity to study $Z\gamma$ production in a more energetic (higher E_T^γ) region, where the sensitivity of this process to bosonic couplings is higher [4, 14]. In addition, this channel is sensitive to anomalous neutrino dipole moments, although a higher integrated luminosity than that available to this study would be required to significantly improve upon LEP results [15].

The measurements of the rate and kinematic properties of $Z\gamma$ production from this study are compared to SM predictions obtained with two higher-order perturbative parton-level calculations at next-to-leading order (NLO) and next-to-next-to-leading order (NNLO) in the strong coupling constant, α_s, as well as with the parton-shower Monte Carlo (MC) simulation. The measured $Z\gamma$ production cross section at high values of the photon E_T is used to search for aTGC ($ZZ\gamma$ and $Z\gamma\gamma$). For these searches an exclusive selection is used, providing higher sensitivity for the anomalous couplings due to further background suppression.

2 ATLAS detector and data samples

2.1 ATLAS detector and experimental data set

The ATLAS detector at the LHC has been described in detail in Ref. [16]. A short overview is presented here, with an emphasis on the subdetectors needed for precision measurement of the $Z(\nu\bar{\nu})\gamma$ final state. The ATLAS detector covers nearly the entire solid angle around the collision point. The major components of the ATLAS detector are an inner tracking detector (ID) surrounded by a thin superconducting solenoid providing a 2 T axial magnetic field, electromagnetic (ECAL) and hadron (HCAL) calorimeters, and a muon spectrometer (MS). The ID is composed of three subsystems. Two detectors cover the pseudorapidity range $|\eta| < 2.5$: the silicon pixel detector and the silicon micro-strip tracker (SCT). The outermost system of the ID, with an acceptance of $|\eta| < 2.0$, is composed of a transition radiation tracker (TRT). The TRT provides identification information for electrons by the detection of transition radiation. The MS is composed of three large superconducting air-core toroid magnets, a system of three stations of chambers for tracking measurements, with high precision in the range $|\eta| < 2.7$, and a muon trigger system covering the range $|\eta| < 2.4$.

The ECAL is composed of alternating layers of passive lead absorber interspersed with active liquid-argon gaps. It covers the range of $|\eta| < 3.2$ and plays a crucial role in photon identification. For $|\eta| < 2.5$ the calorimeter has three longitudinal layers in shower depth, with the first layer having the highest granularity in the η coordinate, and the second layer collecting most of the electromagnetic shower energy for high-p_T objects. A thin presampler layer precedes the ECAL over the range $|\eta| < 1.8$, and is used to correct for the energy lost by EM particles upstream of the calorimeter. The HCAL, surrounding the ECAL, is based on two different technologies, with scintillator tiles or liquid-argon as the active medium, and with either steel, copper, or tungsten as the absorber material. Photons are identified as narrow, isolated showers in the ECAL with no penetration into the HCAL. The fine segmentation of the ATLAS calorimeter system allows efficient separation of jets from isolated prompt photons.

Collision events are selected using a hardware-based first level trigger and a software-based high-level trigger. The resulting recorded event rate from LHC pp collisions at $\sqrt{s} = 13$ TeV during the data-taking period in 2015 and 2016 was approximately 1 kHz [17]. After applying criteria to ensure nominal ATLAS detector operation, the total integrated luminosity useful for data analysis is 36.1 fb^{-1}. The uncertainty in the combined 2015+2016 integrated luminosity is 2.1%. It is derived, following a methodology similar

to that detailed in Ref. [18], from a calibration of the luminosity scale using x–y beam-separation scans performed in August 2015 and May 2016.

2.2 Simulation of signal and backgrounds

Simulated signal and background events are produced with various Monte Carlo event generators, processed through a full ATLAS detector simulation [19] using GEANT4 [20], and then reconstructed with the same procedure used for data. Additional pp interactions (pileup), in the same and neighbouring bunch crossings, are overlaid on the hard scattering process in the MC simulation. The MC events are then reweighted to reproduce the distribution of the number of interactions per bunch crossing observed in data.

In previous $Z\gamma$ publications [2, 4], SHERPA [21] was found to provide a reasonable description of data observed in pp collisions at 7 and 8 TeV in the ATLAS detector. SHERPA 2.2.2 with the NNPDF3.0 NNLO PDF set [22] is used as baseline event generator for the signal modeling in this study. The signal sample is generated with up to three additional final-state partons at leading-order (LO) and up to one additional final-state parton at next-to-leading order (NLO). Alternative signal samples, the first generated using SHERPA 2.1.1 with the CT10 PDF set [23] and the second generated using MG5_aMC@NLO 2.3.3 [24] with the NNPDF3.0 NLO PDF set and interfaced to the PYTHIA 8.212 [25]) parton shower model, are considered for studies of systematic uncertainties. Signal samples with non-zero anomalous triple gauge-boson coupling parameters are also generated using SHERPA 2.1.1 with the CT10 PDF set. The values of parameters used in the generation are given by the expected limits obtained in previous ATLAS study [4].

Background events containing Z bosons with associated jets are simulated using SHERPA 2.1.1 with the CT10 PDF set, while background events containing W bosons with associated jets are simulated using SHERPA 2.2.0 with the NNPDF3.0 NNLO PDF set. For both these processes the matrix elements are calculated for up to 2 partons at NLO and 4 partons at LO. Background events containing a photon with associated jets are simulated using SHERPA 2.1.1 with the CT10 PDF set. Matrix elements are calculated with up to 4 partons at LO. Background events containing a lepton pair and a photon with associated jets are simulated using SHERPA 2.2.2 with NNPDF3.0 NNLO PDF set. Matrix elements including all diagrams with 3 electroweak couplings are calculated for up to 1 parton at NLO and up to 3 partons at LO.

3 Selection of $Z(\nu\bar{\nu})\gamma$ signal events

The event selection criteria are chosen to provide precise cross-section measurements of $Z(\nu\bar{\nu})\gamma$ production and good sensitivity to anomalous gauge-boson couplings between photons and Z bosons. The selection is optimized for obtaining a high signal efficiency together with good background rejection.

Events are required to have been recorded with stable beam conditions and with all relevant detector subsystems operational. Event candidates in both data and MC are selected using the lowest E_{T} unprescaled single photon trigger, which requires the presence of at least one cluster of energy deposition in the ECAL with transverse energy E_{T} larger than 140 GeV. The trigger efficiency is greater than 98% for the photon selection used in this paper.

3.1 Object selection

Photon candidates are reconstructed [26] from ECAL energy clusters with $|\eta| < 2.37$ and $E_{\mathrm{T}} > 150$ GeV. They are classified either as converted (candidates with a matching reconstructed conversion vertex or a matching track consistent with having originated from a photon conversion) or as unconverted (all other candidates). Both kinds of photon candidates are used in analysis. Electron candidates are reconstructed [27] from ECAL energy clusters with $|\eta| < 2.47$ that are associated with a reconstructed track in the ID with transverse momentum $p_{\mathrm{T}} > 7$ GeV. The ECAL cluster of the electron/photon candidate must lie outside the transition region between the barrel and endcap ($1.37 < |\eta| < 1.52$). Muon candidates are reconstructed from tracks in the MS that have been matched to a corresponding track in the inner detector. The combined track is required to have $p_{\mathrm{T}} > 7$ GeV and $|\eta| < 2.7$.

The shower shapes produced in the ECAL are used to identify photons and electrons. Photons are required to pass all the requirements on shower shape variables that correspond to the *Tight* photon identification criteria [28]. Its efficiency ranges from 88% (96%) to 92% (98%) for unconverted (converted) photons with $p_{\mathrm{T}} > 100$ GeV. A sample of "preselected" photons, used for the missing transverse momentum calculation, are required to satisfy less restrictive identification criteria *Loose* of Ref. [28]. Electron candidates are required to pass *Loose* [27] electron identification criteria, whose efficiency is greater than 84%. Muon candidates are required to satisfy *Tight* identification criteria as described in Ref. [29], with efficiency greater than 90% for combined muons used in the selection.

Electron and muon candidates are required to originate from the primary vertex[2] by demanding that the significance of the transverse impact parameter, defined as the absolute value of the track's transverse impact parameter, d_0, measured relative to the beam trajectory, divided by its uncertainty, σ_{d_0}, satisfy $|d_0|/\sigma_{d_0} < 3$ for muons and $|d_0|/\sigma_{d_0} < 5$ for electrons. The difference z_0 between the value of the z coordinate of the point on the track at which d_0 is defined, and the longitudinal position of the primary vertex, is required to satisfy $|z_0 \cdot \sin(\theta)| < 0.5$ mm for both muons and electrons.

Photon, electron and muon candidates are required to be isolated from other particles using the following criteria. The total transverse energy in ECAL energy clusters within $\Delta R = 0.4$ of the photon candidate is required to be less than $2.45\ \mathrm{GeV} + 0.022 \cdot E_{\mathrm{T}}^{\gamma}$, and the sum of the transverse momenta of the tracks located within a distance $\Delta R = 0.2$ of the photon candidate is required to be less than $0.05 \cdot p_{\mathrm{T}}^{\gamma}$. For preselected photons, isolation criteria are not applied. For muons and electrons, the isolation requirement is based on track information and is tuned to have an efficiency of at least 99% [29].

Jets are reconstructed from topological clusters in the calorimeter [30] using the anti-k_t algorithm [31] with a radius parameter of $R = 0.4$. Events with jets arising from detector noise or other non-collision sources are discarded [32]. A multivariate combination of track-based variables is used to suppress jets originating from pile-up in the ID acceptance [33]. The energy of each jet is calibrated and corrected for detector effects using a combination of simulated events and in situ methods [34] using data collected at $\sqrt{s} = 13$ TeV. The selected jets are required to have p_{T} larger than 50 GeV and have $|\eta| < 4.5$.

The missing transverse momentum, $\vec{p}_{\mathrm{T}}^{\,\mathrm{miss}}$, is defined as the negative vector sum of the transverse momenta of all reconstructed physics objects in the event [35] (leptons with $p_{\mathrm{T}} > 7$ GeV, preselected photons with $p_{\mathrm{T}} > 10$ GeV and jets with $p_{\mathrm{T}} > 20$ GeV), plus a "soft term" incorporating tracks from the primary vertex that are not associated with any such objects [36]. The scalar observable $E_{\mathrm{T}}^{\mathrm{miss}}$ is defined to be the

[2] Each primary vertex candidate is reconstructed from at least two associated tracks with $p_{\mathrm{T}} > 0.4$ GeV. The primary vertex is selected among the primary vertex candidates as the one with the highest sum of the squared transverse momenta of its associated tracks.

magnitude of the resulting $\vec{p}_{\mathrm{T}}^{\,\mathrm{miss}}$ vector, and is used as a measure of the total transverse momentum of neutrinos in the event.

To resolve ambiguities in the object reconstruction, the jet candidates lying within $\Delta R < 0.3$ of the photon candidates are removed.

3.2 Signal region definition

The signal region is defined to have exactly one tight isolated photon, as described above. In order to reduce the contamination from events that do not contain high-energy neutrinos (mainly γ + jet background with fake $E_{\mathrm{T}}^{\mathrm{miss}}$ from jet momenta mismeasurements) the selected events are required to have $E_{\mathrm{T}}^{\mathrm{miss}} > 150$ GeV. To reduce the number of $W(\ell\nu)\gamma$ and $Z(\ell\ell)\gamma$ events, a lepton veto is applied: events with any selected electrons or muons are discarded. A cut on the $E_{\mathrm{T}}^{\mathrm{miss}}$ significance, defined as $E_{\mathrm{T}}^{\mathrm{miss}}/\sqrt{\Sigma p_{\mathrm{T}}^{\mathrm{jet}} + E_{\mathrm{T}}^{\gamma}} > 10.5\ \mathrm{GeV}^{1/2}$, further suppresses background contributions with fake $E_{\mathrm{T}}^{\mathrm{miss}}$. An additional angular separation requirement $\Delta\phi(\vec{p}_{\mathrm{T}}^{\,\mathrm{miss}}, \gamma) > \pi/2$ is made, which suppresses the $pp \to W(e\nu) + X$ background. The object and event selections described above define the fiducial region at reconstruction level and are summarized in Table 1.

Photons	Leptons	Jets
$E_T > 150$ GeV	$p_{\mathrm{T}} > 7$ GeV	$p_{\mathrm{T}} > 50$ GeV
$\lvert\eta\rvert < 2.37$,	$\lvert\eta\rvert < 2.47(2.7)$ for $e(\mu)$,	$\lvert\eta\rvert < 4.5$
excluding $1.37 < \lvert\eta\rvert < 1.52$	excluding $1.37 < \lvert\eta^e\rvert < 1.52$	$\Delta R(\mathrm{jet}, \gamma) > 0.3$
Event selection		
$N^{\gamma} = 1$, $N^{\ell} = 0$, $E_{\mathrm{T}}^{\mathrm{miss}} > 150$ GeV, $E_{\mathrm{T}}^{\mathrm{miss}}$ signif. $> 10.5\ \mathrm{GeV}^{1/2}$, $\Delta\phi(\vec{p}_{\mathrm{T}}^{\,\mathrm{miss}}, \gamma) > \pi/2$		
Inclusive : $N_{\mathrm{jet}} \geq 0$, Exclusive : $N_{\mathrm{jet}} = 0$		

Table 1: Definition of the fiducial region. Object selection is presented in the top part of the table, while event selection is described in the bottom part.

4 Background estimation

Backgrounds to the $\nu\bar{\nu}\gamma$ signal originate from several sources. The dominant sources (listed in decreasing order of importance) are estimated with data-driven techniques: non-signal electroweak processes such as $W(\ell\nu)\gamma$, where the lepton is not detected; events with prompt photons and mismeasured jet momenta that gives rise to missing transverse momentum; events with real $E_{\mathrm{T}}^{\mathrm{miss}}$ from neutrinos (such as $Z(\nu\bar{\nu})$ or $W(e\nu)$) and misidentified photons from either electrons or jets. The procedures used to estimate these backgrounds closely follow those of the previous ATLAS measurement [4]. A less important source is $\ell\ell\gamma$ (mainly $\tau\tau\gamma$) production and is estimated with MC simulation. It is expected to contribute roughly 1% of the selected event yield. In the following, each source of background is discussed in detail together with the method used for its estimation.

Misidentified events from $W(\ell\nu)\gamma$ production are one of the dominant background contributions. A large fraction (about 60%) of this contamination arises from $W(\tau\nu)\gamma$ events. Photon+jets events form another

sizable background contribution to the signal region. For the estimation of these backgrounds, two control regions (CRs) are defined by selecting events with the same criteria used for the SR but requiring either exactly one charged lepton (e/μ) in the event, or requiring $E_{\mathrm{T}}^{\mathrm{miss}}$ significance to be less than 10.5 GeV$^{1/2}$. The first CR is enriched with $W(\ell\nu)\gamma$ events (about 77%) while the second CR is enriched with γ+jets events (about 55%). A simultaneous fit to the background-enriched CRs is performed to allow the CRs data to constrain the yield of these main backgrounds by establishing the normalization factors for the $W(\ell\nu)\gamma$ and γ+jets background contribution. The normalization factor for the $W\gamma$ background is found to be close to one, while the normalization factor for the γ+jets background is significantly larger than one, since the pre-fit number is computed at LO, whereas higher order corrections would have considerable impact. The kinematic distributions of these backgrounds are taken from the MC predictions and the individual bins are allowed to float in the fit within their uncertainties. The variation of the background yields due to each of the experimental and MC modeling uncertainties reported in Section 5.1 are treated as Gaussian-distributed nuisance parameters in the likelihood function fit used to obtain the final background predictions in the SR. The dominant systematic uncertainties in the $W(\ell\nu)\gamma$ process come from MC modeling (mostly due to the QCD scale uncertainty) and from the uncertainty on the electron-photon energy scale. Their contributions are 5.8% and 3.8%, respectively. The sytematic uncertainty for γ+jets events is also dominated by the QCD scale component, and amounts to approximately 19%.

Misidentification of electrons as photons also contributes to the background yield in the signal region. The main source of this background is the inclusive $W(e\nu)$ process, but contributions also arise from the single top-quark production and $t\bar{t}$ processes. The estimation of the size of these background contributions is done in two steps. The first is the determination of the probability for an electron to be misidentified as a photon using $Z(e^+e^-)$ decays reconstructed as $e + \gamma$, as described in Ref. [4, 37]. The probability of observing an $e + \gamma$ pair with invariant mass near the Z boson mass is used to determine an electron-to-photon fake factor $f_{e\to\gamma}$. The fake factor is found to vary between 0.6% to 2.7%, depending on the photon's η and p_{T}. The second step is the construction of a control region by applying the nominal $\nu\bar{\nu}\gamma$ selection criteria described in Section 3, with the exception that an electron is required instead of the final-state photon, leading to a control region dominated by the $W(e\nu)$+jets process. The estimated background is then given by the number of events in the chosen control sample scaled by the electron-to-photon fake factor. The statistical uncertainty is determined by the control sample statistics and does not exceed 5%. The systematic uncertainty for this background varies from 13% to 25%, depending on the photon p_{T}, and η and is dominated by the difference between fake rates obtained from $Z(ee)$ and $W(e\nu)$ MC events using generator-level information. The total relative systematic uncertainty of this background estimate is less than 15%, since the main contribution comes from the most populated central pseudorapidity region and has $p_{\mathrm{T}} < 250$ GeV.

To estimate background from the misidentification of jets as photons, a two-dimensional sideband method is used, as described in Ref. [4]. In this method the $\nu\bar{\nu}\gamma$ events are separated into one signal and three control regions. Events in the signal region require the photon to satisfy the nominal photon isolation and tight identification requirements, as described in Section 3. The photon isolation and identification criteria are modified in order to build the control regions, which are disjoint to each other and to the signal region. The modified photon identification criteria requires photons to pass a "non-tight" identification but fail the tight identification. The non-tight selection criteria removes requirements on four out of the nine shower shape variables required for tight photons; the variables that are removed from the list of requirements are those that are least correlated with calorimeter isolation [38]. The number of background events in the signal region can be derived from the number of observed events in the control regions according to the methodology described in Ref. [4]. The statistical uncertainty on the background is defined by the event yields in the four regions, while the systematic uncertainty is 29% and is dominated by the size of

	$N_{\text{jets}} \geq 0$	$N_{\text{jets}} = 0$
$N^{W\gamma}$	650 ± 40 ± 60	360 ± 20 ± 30
$N^{\gamma\text{+jet}}$	409 ± 18 ± 108	219 ± 10 ± 58
$N^{e\to\gamma}$	320 ± 15 ± 45	254 ± 12 ± 35
$N^{\text{jet}\to\gamma}$	170 ± 30 ± 50	140 ± 20 ± 40
$N^{Z(\ell\ell)\gamma}$	40 ± 3 ± 3	26 ± 3 ± 2
$N^{\text{bkg}}_{\text{total}}$	1580 ± 50 ± 140	1000 ± 40 ± 90
$N^{\text{sig}}(\text{exp})$	2328 ± 4 ± 135	1710 ± 4 ± 91
$N^{\text{sig+bkg}}_{\text{total}}$	3910 ± 50 ± 190	2710 ± 40 ± 130
$N^{\text{data}}(\text{obs})$	3812	2599

Table 2: Summary of observed and expected yields (all backgrounds and signal) for events passing the selection requirements in data for the inclusive ($N_{\text{jets}} \geq 0$) and exclusive ($N_{\text{jets}} = 0$) selections. $W\gamma$ and γ+jet backgrounds have been scaled by the normalization factor from the fit, luminosity and cross section. $e \to \gamma$ and jet $\to \gamma$ backgrounds are estimated using data-driven techniques. The row labeled "$N^{\text{sig}}(\text{exp})$" corresponds to the Sherpa NLO prediction. The row labeled "$N^{\text{sig+bkg}}_{\text{total}}$" corresponds to the sum of the expected background contributions and expected signal. The first uncertainty is statistical, while the second is systematic.

changes to the background estimate arising from the variation of the control regions definitions, which lead to changes exceeding size of expected statistical fluctuations. This range also covers possible effects due to the correlation between the isolation and identification criteria..

The resulting signal and background composition is shown in Table 2. Control distributions of the photon transverse energy, missing transverse momentum, and jet multiplicity distributions for the inclusive selection ($N_{\text{jets}} \geq 0$) are shown in Figure 2. Control distributions of the photon transverse energy and the missing transverse momentum distributions for the exclusive selection ($N_{\text{jets}} = 0$) are shown in Figure 3.

Good agreement between data and the SM expectation is observed in the shapes of most of the measured distributions. The discrepancy in the last bin of the inclusive E_T^{γ} distribution, after dedicated checks, was found to be consistent with having arisen from a statistical fluctuation of the data. The uncertainties shown in the figures are treated as being uncorrelated among different systematic sources and different backgrounds.

5 Integrated and differential cross sections

5.1 Description of the cross-section measurements

The number of signal events is determined by subtracting the estimated backgrounds from the number of observed events. The signal yield is then corrected for detection efficiencies in the fiducial region, defined in Table 1. To simplify the interpretation of the results, the cross section is also measured in an extended fiducial region, defined at particle level[3] in Table 3. Compared with the fiducial region, the extended

[3] "Particle level" quantities are defined in terms of stable particles in the MC event record with a proper decay length $c\tau > 10$ mm that are produced from the hard scattering, including those that are the products of hadronization. The particle level jets are

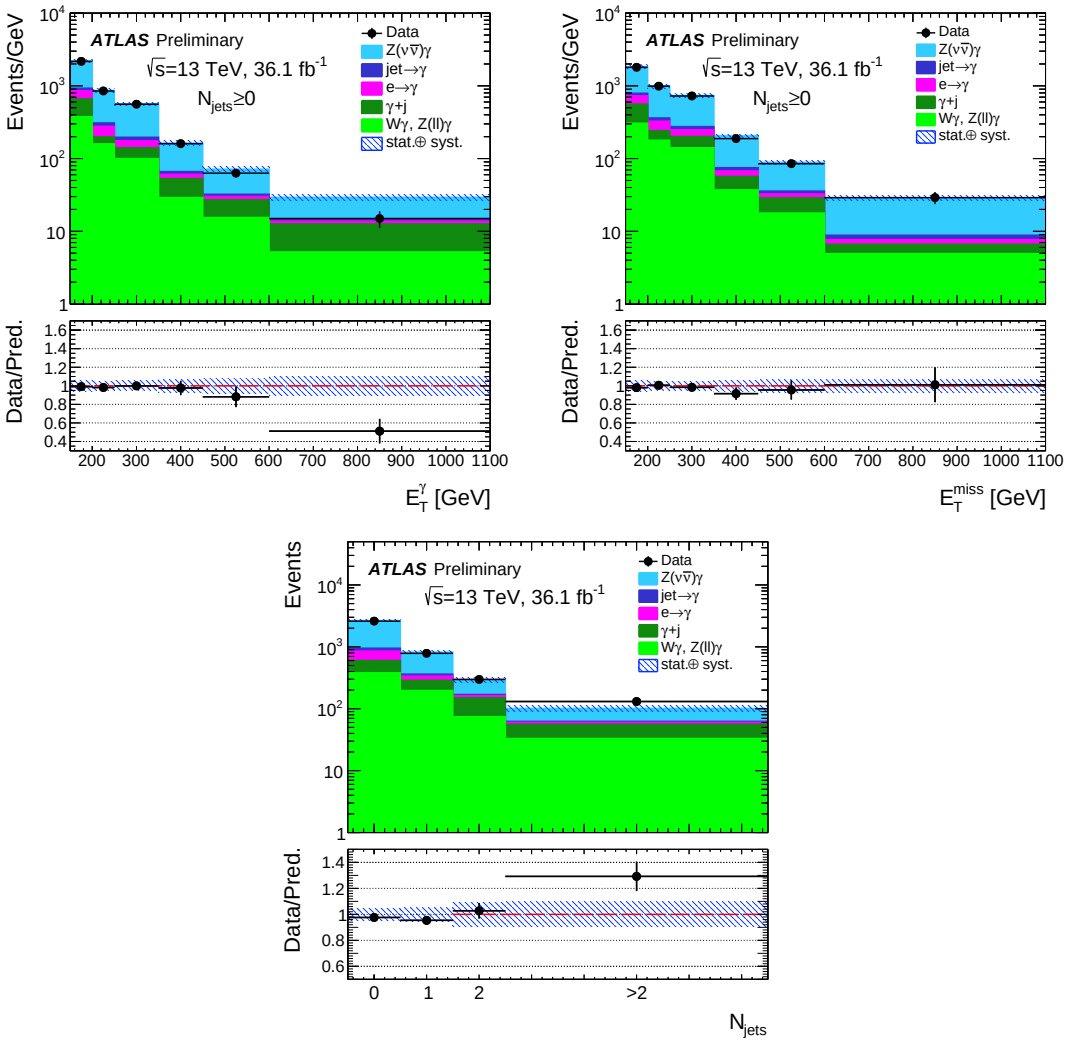

Figure 2: Top left: photon E_{T} distribution; top right: missing transverse energy distribution; bottom: jet multiplicity distribution in the inclusive ($N_{\mathrm{jets}} \geq 0$) signal region. MC expectations are scaled to the integrated luminosity of the data using the expected MC cross sections of each sample. $W\gamma$ and γ+jet backgrounds have been scaled by an additional normalization factor from the fit to data in the corresponding control regions. Backgrounds arising from electron or jet misidentification as a photon are estimated with the data-driven techniques described in the text. The dashed band represents the quadratic sum of systematic and statistical uncertainties of both the background and signal expectation, and includes a contribution arising from the uncertainty on the integrated luminosity of the data sample.

fiducial region removes requirements on $E_{\mathrm{T}}^{\mathrm{miss}}$ significance, $\Delta\phi(\vec{p}_{\mathrm{T}}^{\,\mathrm{miss}}, \gamma)$, the lepton veto and the transition η region for photons.

reconstructed using the anti-k_t algorithm with a radius parameter of $R = 0.4$, using all stable particles except for muons and neutrinos. Particle-level jets in ATLAS do not include muons because jets are built from calorimeter clusters, excluding muons.

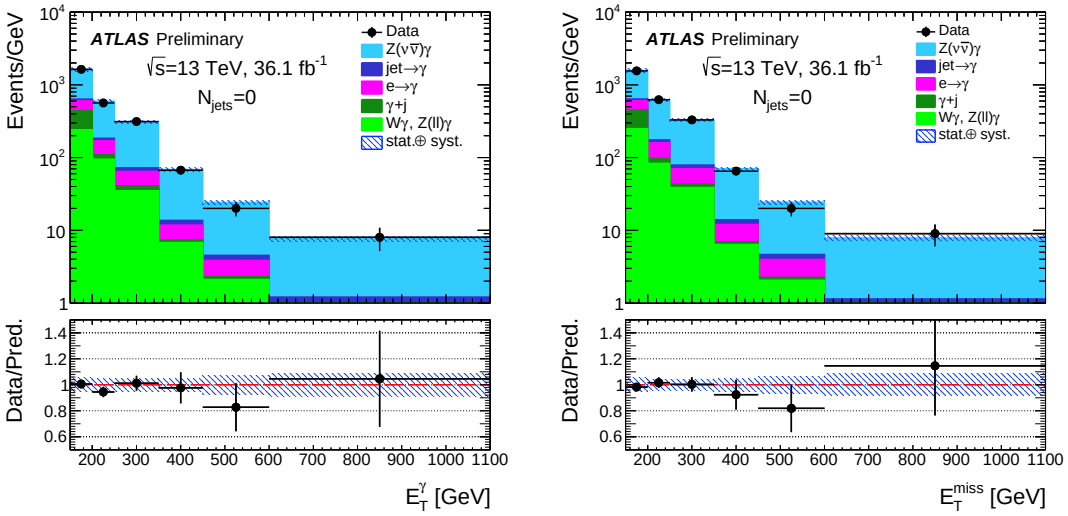

Figure 3: Left: photon E_{T} distribution; right: missing transverse energy distribution in the exclusive ($N_{jets} = 0$) signal region. MC expectations are scaled to the integrated luminosity of the data using the expected MC cross sections of each sample. $W\gamma$ and γ+jet backgrounds have been scaled by an additional normalization factor from the fit to data in the corresponding control regions. Backgrounds arising from electron or jet misidentification as a photon are estimated with the data-driven techniques described in the text. The dashed band represents the quadratic sum of systematic and statistical uncertainties of both the background and signal expectation, and includes a contribution arising from the uncertainty on the integrated luminosity of the data sample.

Category	Requirement
Photons	$E_T^{\gamma} > 150$ GeV
	$\lvert\eta\rvert < 2.37$
Jets	$\lvert\eta\rvert < 4.5$
	$p_T > 50$ GeV
	$\Delta R(\mathrm{jet}, \gamma) > 0.3$
	Inclusive : $N_{\mathrm{jet}} \geq 0$, Exclusive : $N_{\mathrm{jet}} = 0$
Neutrino	$p_T^{\nu\bar{\nu}}$>150 GeV

Table 3: Definition of the extended fiducial region. At particle level $p_T^{\nu\bar{\nu}}$ is the equivalent of $E_{\mathrm{T}}^{\mathrm{miss}}$.

The integrated cross section in the extended fiducial region is calculated as

$$\sigma_{\text{ext-fid}} = \frac{N - B}{A_{Z\gamma} \cdot C_{Z\gamma} \cdot \int Ldt}, \tag{1}$$

where N is the number of candidate events observed, B is the expected number of background events and $\int Ldt$ is the integrated luminosity corresponding to the analyzed dataset. The factors $C_{Z\gamma}$ and $A_{Z\gamma}$ correct for detection efficiency and acceptance, respectively:

- $C_{Z\gamma}$ is defined as the number of reconstructed signal events satisfying all selection criteria divided by the number of events that, at particle level, meet the acceptance criteria of the fiducial region;

	$N_{\text{jets}} \geq 0$	$N_{\text{jets}} = 0$
$A_{Z\gamma}$	0.816 ± 0.029	0.952 ± 0.026
$C_{Z\gamma}$	0.904 ± 0.031	0.889 ± 0.037

Table 4: Summary of values of the correction factors ($C_{Z\gamma}$) and acceptances ($A_{Z\gamma}$) for the $Z\gamma$ cross-section measurements. Uncertainty presented here includes only systematic components, since the statistical uncertainty is found to be negligible.

- $A_{Z\gamma}$ is defined as the number of signal events within the fiducial region divided by the number of signal events within the extended fiducial region, with both numerator and denominator defined at particle level.

The corrections $A_{Z\gamma}$ and $C_{Z\gamma}$ are determined using the $Z\gamma$ signal events generated with Sherpa. In the signal event selection at particle level, the $E_{\text{T}}^{\text{miss}}$ significance and $\Delta\phi(\vec{p}_{\text{T}}^{\,\text{miss}}, \gamma)$ are given by $p_T^{\nu\bar{\nu}}/\sqrt{\Sigma p_{\text{T}}^{\text{jet}} + E_{\text{T}}^{\gamma}}$ and $\Delta\phi(\vec{p}_T^{\,\nu\bar{\nu}}, \gamma)$, respectively. Photon isolation at the particle level is performed using the same requirements and the equivalent cone sizes as described for the reconstruction isolation in the Section 3.1. The numerical values for $A_{Z\gamma}$ and $C_{Z\gamma}$ are summarized in Table 4 along with their uncertainties.

5.2 Systematic uncertainties

Systematic uncertainties in the acceptances $A_{Z\gamma}$ are evaluated by varying the PDF sets, the α_s value, the renormalization and factorization scales (QCD scale uncertainty), and the Monte-Carlo tunes for the parton shower (PS) and multi-parton interactions (MPI). In total, 100 eigenvector sets are checked for the NNPDF3.0 NNLO PDF variation, leading to a relative uncertainty of 0.76% for the inclusive case and 0.35% for the exclusive case. These numbers fully cover variations arising from the use of alternative PDF sets such as CT14 [39] and MMHT2014 [40]. The uncertainty due to imperfect knowledge of α_s is estimated by varying it within the range of its world-average value as provided in Ref. [41] and is found to be negligible. The renormalization and factorization scale uncertainties are assessed by varying these two scales independently by a factor of two from their nominal values, removing combinations where both variations differ by a factor of four, and taking the envelope of the resulting variations. Uncertainties for PS and MPI are evaluated using a series of eigentunes for the Pythia generator with its A14 tune [42]. The size of the renormalization and factorization scale uncertainties does not exceed 3.0%, while PS and MPI uncertainties cause variations from 1.9% to 2.7% for the inclusive and exclusive cases, respectively. The total uncertainties in the acceptance factors are summarized in Table 4.

Systematic uncertainties affecting the correction factor $C_{Z\gamma}$ include contributions arising from uncertainties in the efficiencies of the trigger, reconstruction and particle identification, as well as the uncertainties in the energy, momentum scales and resolutions of the final-state objects. Additional systematic uncertainty sources are related to the modeling of particle spectra and pileup events. Spectrum modeling uncertainties are estimated by the variation of the PDF set and QCD scales as described above for the case of the acceptance factor A. Some of these contributions are found to have a nonlinear dependence on photon transverse energy, $E_{\text{T}}^{\text{miss}}$ or jet multiplicity. In these cases, uncertainties estimated as a function of these observables are used in the unfolding process of Section 5.5 when the corresponding kinematic distributions are derived from the signal sample. Table 5 displays the size of the individual contributions to the uncertainties in the $C_{Z\gamma}$ factor; the total uncertainty is summarized in Table 4.

Source	Relative uncertainty in [%]	
	$N_{\text{jets}} \geq 0$	$N_{\text{jets}} = 0$
Trigger efficiency	0.79	0.79
Photon identification efficiency	1.5	1.5
Photon isolation efficiency	0.48	0.47
Electron-photon energy scale	2.5	2.5
Electromagnetic energy resolution	0.11	0.09
Jet energy scale	0.92	2.2
Jet energy resolution	0.10	0.43
$E_{\text{T}}^{\text{miss}}$ energy scale	<0.1	<0.1
$E_{\text{T}}^{\text{miss}}$ energy resolution	0.13	<0.1
Pileup simulation	0.85	1.1
Spectrum modeling	1.3	1.3
Sum	3.5	4.2

Table 5: Relative systematic uncertainties on the signal correction factor $C_{Z\gamma}$ for the inclusive and exclusive $Z\gamma$ measurement.

5.3 Integrated extended fiducial cross section

The measurements of the cross sections, along with their uncertainties, are based on the maximization of the profile-likelihood ratio

$$\Lambda(\sigma) = \frac{\mathcal{L}(\sigma, \hat{\hat{\boldsymbol{\theta}}}(\sigma))}{\mathcal{L}(\hat{\sigma}, \hat{\boldsymbol{\theta}})}, \tag{2}$$

where $\mathcal{L}$ represents the likelihood function, σ is the cross section, and $\boldsymbol{\theta}$ are the nuisance parameters corresponding to the sources of systematic uncertainty. The $\hat{\sigma}$ and $\hat{\boldsymbol{\theta}}$ terms denote the unconditional maximum-likelihood estimate of the parameters, i.e., the parameters for which the likelihood is maximized for both σ and $\boldsymbol{\theta}$. $\hat{\hat{\boldsymbol{\theta}}}(\sigma)$ denotes the value of $\boldsymbol{\theta}$ that maximizes $\mathcal{L}$ for a given values of σ.

The likelihood function is defined as

$$\mathcal{L}(\sigma, \boldsymbol{\theta}) = \text{Poisson}(N \mid S(\sigma, \boldsymbol{\theta}) + B(\boldsymbol{\theta})) \cdot \text{Gaussian}(\boldsymbol{\theta_0} \mid \boldsymbol{\theta}), \tag{3}$$

representing the product of the Poisson probability of observing N events, given expectations of S for the signal and B for the background, multiplied by the Gaussian constraints $\boldsymbol{\theta}$ on the systematic uncertainties, with central values $\boldsymbol{\theta_0}$ from auxiliary measurements, as described in Section 5.1.

The measured cross sections for $Z(\nu\bar{\nu})\gamma$ production in the extended fiducial region are summarized in Table 6, along with the theoretical predictions of the MCFM generator described in Section 5.4. The measured cross sections agree with the SM expectations to within one standard deviation. Systematic uncertainties arise from uncertainties in the acceptances and correction factors, as well as from uncertainties in the background estimates. These two sources contribute roughly equally to the uncertainty on the measured cross sections. Compared with the $Z\gamma$ measurements at $\sqrt{s} = 8$ TeV [4], the systematic

$\sigma^{\text{ext.fid.}}$ [fb]	$\sigma^{\text{ext.fid.}}$ [fb]
Measurement	NNLO MCFM Prediction
$N_{\text{jets}} \geq 0$	
$83.7^{+3.6}_{-3.5}$ (stat.)$^{+6.9}_{-6.2}$ (syst.)$^{+1.7}_{-2.0}$ (lumi.)	78.1 ± 0.2(stat.)± 4.4(syst.)
$N_{\text{jets}} = 0$	
$52.4^{+2.4}_{-2.3}$ (stat.)$^{+4.0}_{-3.6}$ (syst.)$^{+1.2}_{-1.1}$ (lumi.)	55.9 ± 0.1(stat.)± 2.5(syst.)

Table 6: Measured cross sections for $Z(\nu\bar{\nu})\gamma$ production within the extended fiducial region for a centre-of-mass energy of $\sqrt{s} = 13$ TeV, with corresponding SM expectations obtained at next-to-next-to-leading order in the strong coupling constant α_s from the MCFM [44] generator.

uncertainty is significantly reduced. This improvement is due primarily to the reduction of systematic uncertainty allowed by the data-driven estimate of the γ+jets and $W\gamma$ backgrounds.

An additional check of the theoretical predictions is done with the MATRIX generator [43]. Cross sections obtained by MATRIX (inclusive case: $\sigma^{\text{ext.fid.}}$=78.6 ± 0.4 ± 4.1 fb, exclusive case: $\sigma^{\text{ext.fid.}}$=55.8 ± 0.3 ± 2.1 fb) and MCFM are found to be in agreement within their statistical uncertainty.

5.4 Standard Model predictions

The resulting measurement of the rate and kinematic distributions of $Z\gamma$ production is compared to SM expectations using the parton shower Monte Carlo SHERPA and the NNLO parton level generators MCFM and MATRIX. The NNPDF30 PDF set is used for the SHERPA, MCFM and MATRIX generation. The values of the renormalization and factorization scales are set to $m_{Z\gamma}$ for the MCFM and MATRIX NNLO generation of the $Z\gamma$ process.

Photon isolation criterion at the parton level is applied by considering a cone of variable opening ΔR (with maximum opening ΔR_{max}=0.1) centred around the photon direction, and requiring that the transverse energy flow inside that cone be always less that a given fraction of the photon p_T; such fraction is set to 0.1 when ΔR=ΔR_{max}, and smoothly tends to zero when $\Delta R \to 0$, as described in Ref. [45]. Due to this procedure, the contribution from photon fragmentation to the NNLO calculations of the MCFM and MATRIX SM predictions is zero.

Events generated with SHERPA, as described in Section 2.2, are also compared to the particle-level measurements. For the NNLO parton level predictions, parton-to-particle correction factors $C^{*(\text{parton}\to\text{particle})}$ must be applied in order to obtain the particle level cross sections. These correction factors are computed as the ratios of the $pp \to Z\gamma$ cross sections predicted by SHERPA with hadronization and the underlying event disabled to the cross sections with them enabled. The systematic uncertainty in the correction factors is evaluated by using a signal sample from an alternative generator MG5_aMC@NLO, taking the resulting change in $C^{*(\text{parton}\to\text{particle})}$ as the one-sided size of a symmetrized value for the uncertainty. This accounts for uncertainties in both the parton shower modeling and the description of the underlying event. The value of $C^{*(\text{parton}\to\text{particle})}$ is found to be 0.87 ± 0.04 for the inclusive measurement and 0.97 ± 0.04 for the exclusive measurement. For the exclusive measurement, the parton-to-particle correction includes an additional contribution from the jet veto, which compensates the difference in the photon isolation between the parton and particle levels. The particle level cross sections are then obtained by multiplying

the NNLO parton level cross section values by the $C^{*(\text{parton}\to\text{particle})}$ correction factors, and are displayed in the Table 6.

The systematic uncertainty on the expected NNLO SM cross sections arising from uncertainties on the QCD scale is estimated by varying the QCD scales by factors of 0.5 and 2.0 (separately for the renormalization and factorization scales). The systematic uncertainty due to the PDF choice is computed using the eigenvectors of the NNPDF 3.0 PDF set [22] and the envelope of the differences between the results obtained with the CT14 [39], MMHT2014 [40] PDF sets, according to the PDF4LHC recommendations [46]. MATRIX predictions do not include systematic uncertainty due to the PDF choice.

5.5 Differential extended fiducial cross section

The measurement of the $Z\gamma$ production differential cross sections allows a comparison of experimental results with SM expectations in terms of both the absolute rates and the shapes of kinematic distributions. The measurements are performed as a function of several observables that are sensitive to higher-order perturbative QCD corrections [47] and to a possible manifestation of aTGCs: photon transverse energy E_{T}^{γ}, transverse momentum of neutrino-antineutrino pair $p_{\mathrm{T}}^{\nu\bar{\nu}}$, and jet multiplicity N_{jets}. The differential cross sections are defined in the extended fiducial region, and are extracted with an unfolding procedure that corrects for measurement inefficiencies and resolution effects that modify the observed distributions. The procedure described in Ref. [4] is followed, using an iterative Bayesian method [48]. For each distribution, events from simulated signal MC samples are used to generate a response matrix that accounts for bin-to-bin migration effects between the reconstructed and particle level distributions.

The statistical uncertainties of the unfolded distributions are estimated using pseudo-experiments, generated by fluctuating each bin of the observed spectrum according to a Poisson distribution with a mean value equal to the observed yield. The shape uncertainties arising from the limited statistics of the signal MC sample are also obtained by generating pseudo-experiments. The sources of systematic uncertainty are discussed in Section 5.1, with their impact on the unfolded distribution assessed by varying the response matrix for each of the systematic uncertainty sources by one standard deviation and combining the resulting differences from the nominal values in quadrature.

The differential cross sections with respect to E_{T}^{γ} and $p_{\mathrm{T}}^{\nu\bar{\nu}}$ are shown in Figures 4 and 5, respectively, for both the inclusive and exclusive measurements. Figure 6 shows the cross section measured in bins of jet multiplicity. The values of the SM expectations shown in the figures are obtained as described in Section 5.4.

Good agreement with SM expectations is observed in all but the last bin of the E_T^{γ} inclusive distribution. This disagreement is a consequence of the corresponding disagreement observed in Figure 2, which was found to be consistent with having arisen from a statistical fluctuation of the data.

6 Limits on triple gauge boson couplings

Vector-boson couplings are completely fixed within the Standard Model by the $\mathrm{SU}(2)_L\times\mathrm{U}(1)_Y$ gauge structure. Their determination is thus a crucial test of the model. Any deviation from the SM prediction is referred to as an anomalous coupling.

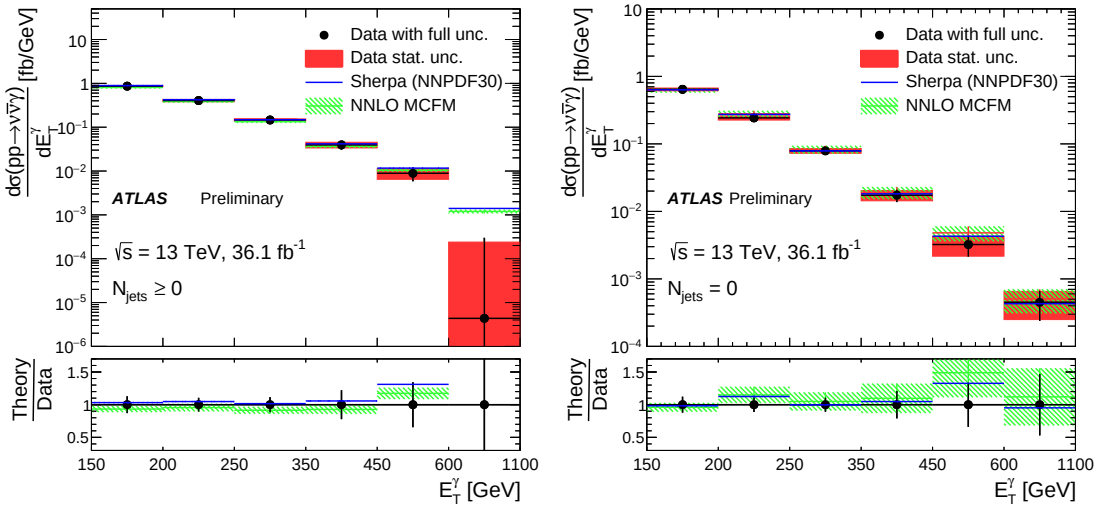

Figure 4: The measured (points with error bars) and predicted differential cross sections as a function of E_{T}^{γ} for the $pp \to \nu\bar{\nu}\gamma$ process in the inclusive $N_{\mathrm{jets}} \geq 0$ (left) and exclusive $N_{\mathrm{jets}} = 0$ (right) extended fiducial regions. The error bars on the data points show the quadratic combination of the statistical and systematic uncertainties. The MCFM NNLO predictions are shown with shaded bands that indicate the theoretical uncertainties described in Section 5.4. The SHERPA predictions are shown with shaded bands indicating the statistical uncertainties from the size of the MC samples (too small to be visible). The lower plots show the ratios of the SM expectation to the measured values (shaded bands), with the error bars on the points showing the relative uncertainties in the experimental measurements. The bin size varies from 50 GeV to 500 GeV.

Within the framework of the effective vertex function approach [49], anomalous triple gauge-boson coupling contributions to $Z\gamma$ production can be parameterized by four CP-violating (h_1^V, h_2^V) and four CP-conserving (h_3^V, h_4^V) complex parameters. Here $V = Z$, γ, and the h_i^Z and h_i^γ are the parameters of $ZZ\gamma$ and $Z\gamma\gamma$ vertices, respectively. The $h_3^V(h_1^V)$ and $h_4^V(h_2^V)$ parameters correspond to the electric (magnetic) dipole and magnetic (electric) quadrupole transition moments of V, respectively [50].

All of these parameters are zero at tree level in the SM. Since the CP-conserving couplings $h_{3,4}^V$ do not interfere with the CP-violating couplings $h_{1,2}^V$, and their sensitivities to aTGCs are nearly identical [49], the limits from this study are expressed solely in terms of the CP-conserving parameters $h_{3,4}^V$.

The yields of $Z\gamma$ events with high E_{T}^{γ} from the exclusive (zero-jet) selection are used to set limits on $h_{3,4}^V$. The exclusive selection is used because it significantly reduces the SM contribution at high E_{T}^{γ} and therefore optimizes the sensitivity to anomalous couplings. The contribution from aTGCs increases with the E_{T} of the photon, and the measurement of $Z\gamma$ production is found to have the highest sensitivity to aTGCs by restricting the search to the portion of the extended fiducial region with E_{T}^{γ} greater than 600 GeV.

Cross-section values modified by the inclusion of aTGCs ($\sigma_{Z\gamma}^{\mathrm{aTGC}}$) are obtained from the MCFM generator. These values are displayed in Table 7 for several combinations of choices of the $ZZ\gamma$ vertex parameters h_3^Z and h_4^Z.

The number of expected $Z\gamma$ events in the exclusive aTGC region ($N_{Z\gamma}^{\mathrm{aTGC}}(h_3^V, h_4^V)$, where $V = Z$ or γ) is

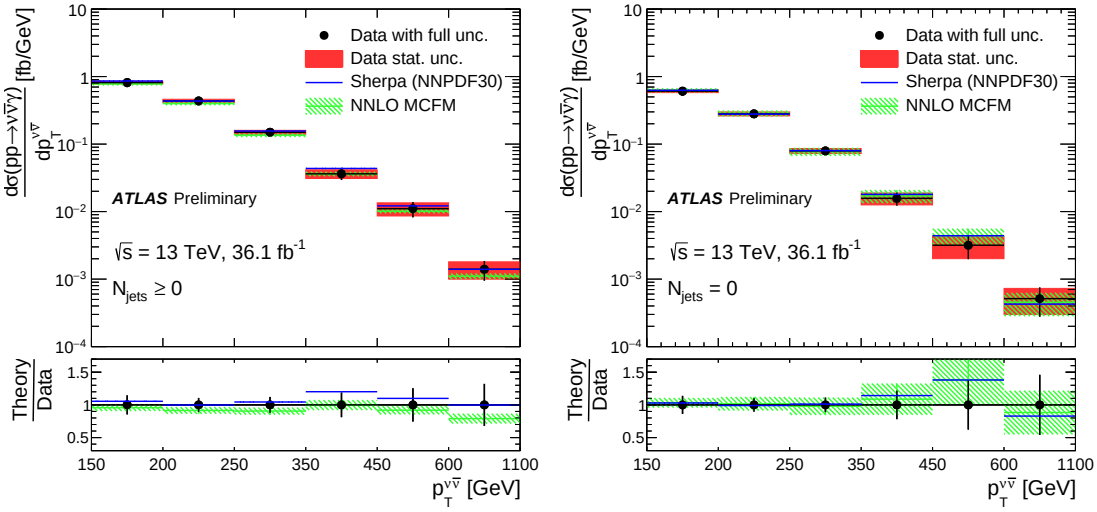

Figure 5: The measured (points with error bars) and predicted differential cross sections as a function of $p_{\mathrm{T}}^{\nu\bar{\nu}}$ for the $pp \to \nu\bar{\nu}\gamma$ process in the inclusive $N_{\mathrm{jets}} \geq 0$ (left) and exclusive $N_{\mathrm{jets}} = 0$ (right) extended fiducial regions. The error bars on the data points show the quadratic combination of the statistical and systematic uncertainties. The MCFM NNLO predictions are shown with shaded bands that indicate the theoretical uncertainties described in Section 5.4. The SHERPA predictions are shown with shaded bands indicating the statistical uncertainties from the size of the MC samples (too small to be visible). The lower plots show the ratios of the SM expectation to the measured values (shaded bands), with the error bars on the points showing the relative uncertainties in the experimental measurements. The bin size varies from 50 GeV to 500 GeV.

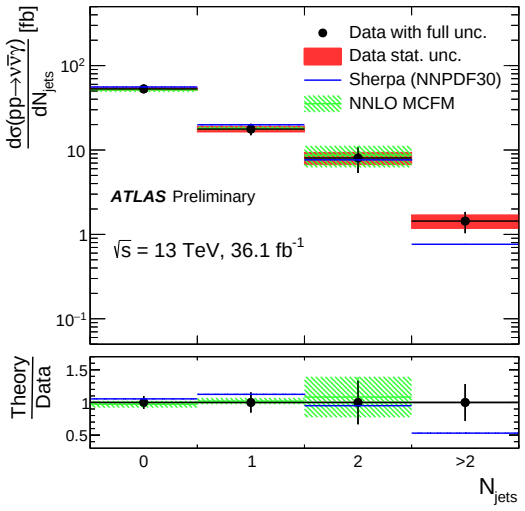

Figure 6: The measured (points with error bars) and predicted cross sections as a function of N_{jets} for the $pp \to \nu\bar{\nu}\gamma$ process in the extended fiducial region. The error bars on the data points show the quadratic combination of the statistical and systematic uncertainties. The MCFM NNLO predictions are shown with shaded bands that indicate the theoretical uncertainties described in Section 5.4. The SHERPA predictions are shown with shaded bands indicating the statistical uncertainties from the size of the MC samples (too small to be visible). The lower plots show the ratios of the SM expectation to the measured values (shaded bands), with the error bars on the points showing the relative uncertainties in the experimental measurements.

h_3^Z \ h_4^Z	−0.0000005	0	0.0000005
−0.0005	0.439	0.696	1.42
0	0.477	0.243	0.483
0.0005	1.40	0.674	0.424

Table 7: Cross section [fb] for the exclusive $Z(\rightarrow \nu\bar{\nu})\gamma$ process, requiring a photon with $E_T^\gamma > 600$ GeV, for different values of h_3^Z (vertical), and h_4^Z (horizontal). For the Standard Model with no anomalous triple gauge couplings, $h_3^Z = h_4^Z = 0$.

obtained using

$$N_{Z\gamma}^{\text{aTGC}}(h_3^V, h_4^V) = \sigma_{Z\gamma}^{\text{aTGC}}(h_3^V, h_4^V) \times C_{Z\gamma} \times A_{Z\gamma} \times C^{*(\text{parton}\rightarrow\text{particle})} \times \int \mathcal{L} dt. \quad (4)$$

The anomalous couplings influence the kinematic properties of the $Z\gamma$ events and thus the efficiency factor of the event reconstruction ($C_{Z\gamma}$). The maximum variation of $C_{Z\gamma}$ due to non-zero aTGC parameters within the measured aTGC limits (about 7%) is adopted as an additional systematic uncertainty. The effect of anomalous couplings on the acceptance factor ($A_{Z\gamma}$) and parton-to-particle factor ($C^{*(\text{parton}\rightarrow\text{particle})}$) is an order of magnitude smaller than that on $C_{Z\gamma}$, and so is neglected.

Limits on a given aTGC parameter are extracted from a frequentist profile-likelihood test similar to that of Section 5.3. The profile likelihood depends on the observed number of exclusive $Z\gamma$ candidate events, the amount of expected signal as a function of aTGC given by Equation 4, and the estimated number of background events. A point in the aTGC space is accepted (rejected) at the 95% confidence level (C.L.) if fewer (more) than 95% of randomly generated pseudo-experiments exhibit larger profile-likelihood ratio values than that observed in data. In this context, a pseudo-experiment is a set of randomly generated numbers of events that follow a Poisson distribution with mean equal to the sum of the number of expected signal events and the estimated number of background events. Systematic uncertainties are incorporated into the likelihood function via a set of nuisance parameters with correlated Gaussian constraints. All nuisance parameters are allowed to fluctuate in the pseudo-experiments.

The allowed 95% C.L. ranges for the anomalous couplings are shown in Table 8 for $ZZ\gamma$ (h_3^Z and h_4^Z) and $Z\gamma\gamma$ (h_3^γ and h_4^γ) vertices. No evidence of anomalous couplings is observed. Limits on anomalous couplings imposed by this analysis are 3–7 times more stringent than those of prior studies, which range between $0.8–1.0 \times 10^{-3}$ for h_3^γ, h_3^Z and between $2.9–3.2 \times 10^{-6}$ for h_4^γ, h_4^Z [4].

Limits on possible combinations of each pair of aTGC are also evaluated. The 95% C.L. allowed regions are shown as contours on the (h_3^γ, h_4^γ) and (h_3^Z, h_4^Z) planes in Figure 7, which are the only such pairs that are expected to interfere [49].

Allowed ranges are also determined for parameters of the effective field theory (EFT) of Ref. [51], which includes four dimension-8 operators describing aTGC interactions of neutral gauge bosons. The coefficients of these operators are denoted $C_{\widetilde{B}W}/\Lambda^4$, C_{BW}/Λ^4, C_{WW}/Λ^4 and C_{BB}/Λ^4, as described in Ref. [52]. Λ is a parameter with the dimension of mass that is associated with the energy scale of the new physics described by the EFT. The 95% C.L. limits on these EFT parameters displayed in Table 9

Parameter	Limit 95% C.L.	
	Measured	Expected
h_3^γ	$(-3.7 \times 10^{-4}, 3.7 \times 10^{-4})$	$(-4.2 \times 10^{-4}, 4.3 \times 10^{-4})$
h_3^Z	$(-3.2 \times 10^{-4}, 3.3 \times 10^{-4})$	$(-3.8 \times 10^{-4}, 3.8 \times 10^{-4})$
h_4^γ	$(-4.4 \times 10^{-7}, 4.3 \times 10^{-7})$	$(-5.1 \times 10^{-7}, 5.0 \times 10^{-7})$
h_4^Z	$(-4.5 \times 10^{-7}, 4.4 \times 10^{-7})$	$(-5.3 \times 10^{-7}, 5.1 \times 10^{-7})$

Table 8: Observed and expected one dimensional 95% C.L. limits on h_3^γ, h_3^Z, h_4^γ and h_4^Z, under the assumption that any observed excess in data relative to the associated background estimate is due solely to h_3^V or h_4^V. For each row, all parameters other than the one under study are set to 0.

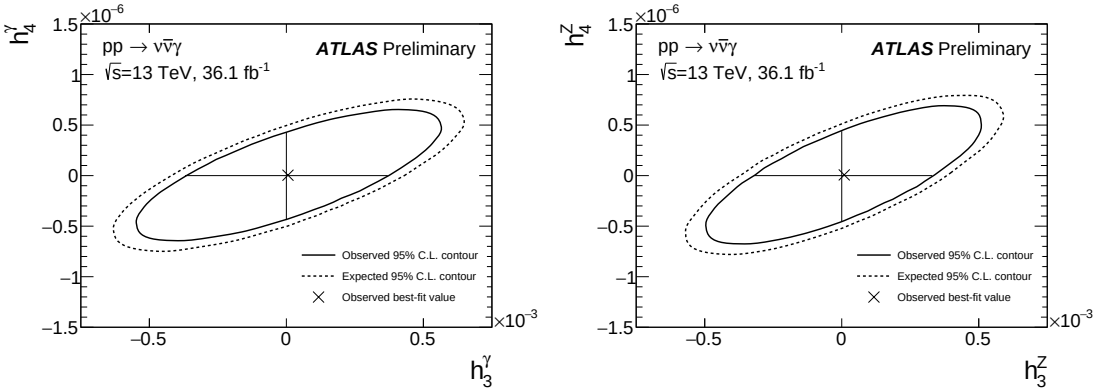

Figure 7: Observed (solid ellipse) and expected (dashed ellipse) 95% C.L. contours in the two-parameter planes of the pairs of anomalous couplings h_3^γ and h_4^γ (left) and h_3^Z and h_4^Z (right). The horizontal and vertical lines inside each contour correspond to the limits found in the one-parameter fit procedure, while the orientation of the ellipses indicate the correlations between the parameters in the two-dimensional fit. In each case, the two parameters not being displayed are set to 0.

are derived from the limits of Table 8 making use of a linear transformation relating the EFT and vertex function aTGC parameters.

Parameter	Limit 95% C.L.	
	Measured [TeV^{-4}]	Expected [TeV^{-4}]
$C_{\widetilde{B}W}/\Lambda^4$	$(-1.1, 1.1)$	$(-1.3, 1.3)$
C_{BW}/Λ^4	$(-0.65, 0.64)$	$(-0.74, 0.74)$
C_{WW}/Λ^4	$(-2.3, 2.3)$	$(-2.7, 2.7)$
C_{BB}/Λ^4	$(-0.24, 0.24)$	$(-0.28, 0.27)$

Table 9: Observed and expected one dimensional 95% C.L. limits on $C_{\widetilde{B}W}/\Lambda^4$, C_{BW}/Λ^4, C_{WW}/Λ^4 and C_{BB}/Λ^4 EFT parameters, under the assumption that any excess in data over background predictions is due solely to $C_{\widetilde{B}W}/\Lambda^4$, C_{BW}/Λ^4, C_{WW}/Λ^4 or C_{BB}/Λ^4. For each row, all parameters other than the one under study are set to 0.

7 Conclusion

The cross section for the production of a Z boson in association with an isolated high-energy photon is measured using 36.1 fb^{-1} of pp collisions at $\sqrt{s}$ = 13 TeV collected with the ATLAS detector at the LHC. The analysis uses the invisible decay mode $Z \to \nu\bar{\nu}$ of the Z boson, and is performed in a fiducial phase space closely matching the detector acceptance.

Kinematic distributions are presented in terms of differential cross sections with respect to the transverse energy of the photon, the missing transverse energy, and the jet multiplicity, and are compared to the SM expectations. Measurements are made for both the inclusive case, with no requirements on the recoil system, and the exclusive case in which no jets with $p_{\mathrm{T}} > 50$ GeV are allowed within $|\eta| < 4.5$.

The data are compared to SM expectation derived from a parton shower Monte Carlo (Sherpa) and from parton-level perturbative calculations carried out at NNLO (Mcfm and Matrix). Good agreement is observed between the measured and expected total and differential cross sections.

In the absence of significant deviations from SM expectations, the data are used to set limits on anomalous couplings of photons and Z bosons. Limits on aTGCs are determined using a modified SM Lagrangian that includes operators proportional to the h_3^V and h_4^V ($V = Z$ or γ) parameters of the vertex function parametrization of aTGC contributions to $Z\gamma$ production. The limits are also transformed into limits on the $C_{\widetilde{B}W}/\Lambda^4$, C_{BW}/Λ^4, C_{WW}/Λ^4 and C_{BB}/Λ^4 parameters of an effective field theory formulation of aTGC effects. The limits obtained from the current study are 3–7 times better than those available prior to this study.

References

[1] ATLAS Collaboration, *Measurement of $W\gamma$ and $Z\gamma$ production in proton–proton collisions at $\sqrt{s}$ = 7 TeV with the ATLAS detector*, JHEP **09** (2011) 072, arXiv: 1106.1592 [hep-ex].

[2] ATLAS Collaboration, *Measurements of $W\gamma$ and $Z\gamma$ production in pp collisions at $\sqrt{s}$ = 7 TeV with the ATLAS detector at the LHC*, Phys. Rev. D **87** (2013) 112003, arXiv: 1302.1283 [hep-ex], Erratum: Phys. Rev. D **91** (2015) 119901.

[3] CMS Collaboration, *Measurement of the $Z\gamma$ Production Cross Section in pp Collisions at 8 TeV and Search for Anomalous Triple Gauge Boson Couplings*, JHEP **1504** (2015) 164, arXiv: 1502.05664 [hep-ex].

[4] ATLAS Collaboration, *Measurements of $Z\gamma$ and $Z\gamma\gamma$ production in pp collisions at $\sqrt{s}$ = 8 TeV with the ATLAS detector*, Phys. Rev. D **93** (2016) 112002, arXiv: 1604.05232 [hep-ex].

[5] L3 Collaboration, P. Achard et al., *Study of the $e^+e^- \to Z\gamma$ process at LEP and limits on triple neutral-gauge-boson couplings*, Phys. Lett. B **597** (2004) 119, arXiv: hep-ex/0407012 [hep-ex].

[6] DELPHI Collaboration, J. Abdallah et al., *Study of triple-gauge-boson couplings ZZZ, $ZZ\gamma$ and $Z\gamma\gamma$ at LEP*, Eur. Phys. J. C **51** (2007) 525, arXiv: 0706.2741 [hep-ex].

[7] OPAL Collaboration, G. Abbiendi et al., *Search for trilinear neutral gauge boson couplings in $Z\gamma$ production at $\sqrt{s}$ = 189 GeV at LEP*, Eur. Phys. J. C **17** (2000) 553, arXiv: hep-ex/0007016.

[8] OPAL Collaboration, G. Abbiendi et al., *Constraints on anomalous quartic gauge boson couplings from nu anti-nu gamma gamma and q anti-q gamma gamma events at LEP-2*, Phys. Rev. D **70** (2004) 032005, arXiv: hep-ex/0402021.

[9] D0 Collaboration, V. M. Abazov et al., *$Z\gamma$ production and limits on anomalous $ZZ\gamma$ and $Z\gamma\gamma$ couplings in $p\bar{p}$ collisions at $\sqrt{s}$ = 1.96 TeV*, Phys. Rev. D **85** (2012) 052001, arXiv: 1111.3684 [hep-ex].

[10] D0 Collaboration, V. M. Abazov et al., *Measurement of the $Z\gamma \to \nu\bar{\nu}\gamma$ cross section and limits on anomalous $ZZ\gamma$ and $Z\gamma\gamma$ couplings in $p\bar{p}$ collisions at $\sqrt{s}$ = 1.96 TeV*, Phys. Rev. Lett. **102** (2009) 201802, arXiv: 0902.2157 [hep-ex].

[11] CDF Collaboration, T. Aaltonen et al., *Limits on Anomalous Trilinear Gauge Couplings in $Z\gamma$ Events from $p\bar{p}$ Collisions at $\sqrt{s}$ = 1.96 TeV*, Phys. Rev. Lett. **107** (2011) 051802, arXiv: 1103.2990 [hep-ex].

[12] A. Arbey, *Fundamental Composite Electroweak Dynamics: Status at the LHC*, Phys. Rev. D **95** (2017) 015028, arXiv: 1502.04718 [hep-ph].

[13] G. J. Gounaris, *New and standard physics contributions to anomalous Z and γ self-couplings*, Phys. Rev. D **62** (2000) 073013, arXiv: hep-ph/0003143.

[14] ATLAS Collaboration, *Studies of $Z\gamma$ production in association with a high-mass dijet system in pp collisions at $\sqrt{s}$ = 8 TeV with the ATLAS detector*, JHEP **07** (2017) 107, arXiv: 1705.01966 [hep-ex].

[15] A. Gutierrez-Rodriguez, M. Koksal, A. A. Billur and M. A. Hernandez-Ruiz, *Studies on the anomalous magnetic and electric dipole moments of the tau-neutrino in pp collisions at the LHC*, (2017), arXiv: 1712.02439 [hep-ph].

[16] ATLAS Collaboration, *The ATLAS Experiment at the CERN Large Hadron Collider*, JINST **3** (2008) S08003.

[17] ATLAS Collaboration, *Performance of the ATLAS Trigger System in 2015*, Eur. Phys. J. C **77** (2017) 317, arXiv: 1611.09661 [hep-ex].

[18] ATLAS Collaboration, *Luminosity determination in pp collisions at $\sqrt{s}$ = 8 TeV using the ATLAS detector at the LHC*, Eur. Phys. J. C **76** (2016) 653, arXiv: 1608.03953 [hep-ex].

[19] ATLAS Collaboration, *The ATLAS Simulation Infrastructure*, Eur. Phys. J. C **70** (2010) 823, arXiv: 1005.4568 [physics.ins-det].

[20] S. Agostinelli et al., *GEANT4: A simulation toolkit*, Nucl. Instrum. Meth. A **506** (2003) 250.

[21] T. Gleisberg, S. Hoeche, F. Krauss, M. Schonherr, S. Schumann et al., *Event generation with SHERPA 1.1*, JHEP **02** (2009) 007, arXiv: 0811.4622 [hep-ph].

[22] R. D. Ball et al., *Parton distributions for the LHC Run II*, JHEP **04** (2015) 040, arXiv: 1410.8849 [hep-ph].

[23] H.-L. Lai et al., *New parton distributions for collider physics*, Phys. Rev. D **82** (2010) 074024, arXiv: 1007.2241 [hep-ph].

[24] J. Alwall et al., *The automated computation of tree-level and next-to-leading order differential cross sections, and their matching to parton shower simulations*, JHEP **07** (2014) 079, arXiv: 1405.0301 [hep-ph].

[25] T. Sjostrand, S. Mrenna and P. Z. Skands, *A Brief Introduction to PYTHIA 8.1*, Comput. Phys. Commun. **178** (2008) 852, arXiv: 0710.3820 [hep-ph].

[26] ATLAS Collaboration, *Measurement of the photon identification efficiencies with the ATLAS detector using LHC Run-1 data*, Eur. Phys. J. C **76** (2016) 666, arXiv: 1606.01813 [hep-ex].

[27] ATLAS Collaboration, *Electron efficiency measurements with the ATLAS detector using the 2015 LHC proton–proton collision data*, ATLAS-CONF-2016-024, 2016, URL: https://cds.cern.ch/record/2157687.

[28] ATLAS Collaboration, *Photon identification in 2015 ATLAS data*, ATL-PHYS-PUB-2016-014, 2016, URL: https://cds.cern.ch/record/2203125.

[29] ATLAS Collaboration, *Muon reconstruction performance of the ATLAS detector in proton–proton collision data at $\sqrt{s}$ = 13 TeV*, Eur. Phys. J. C **76** (2016) 292, arXiv: 1603.05598 [hep-ex].

[30] ATLAS Collaboration, *Topological cell clustering in the ATLAS calorimeters and its performance in LHC Run 1*, Eur. Phys. J. C **77** (2017) 490, arXiv: 1603.02934 [hep-ex].

[31] M. Cacciari, G. P. Salam and G. Soyez, *The Anti-k(t) jet clustering algorithm*, JHEP **04** (2008) 063, arXiv: 0802.1189 [hep-ph].

[32] ATLAS Collaboration, *Selection of jets produced in 13 TeV proton–proton collisions with the ATLAS detector*, ATLAS-CONF-2015-029, 2015, URL: https://cds.cern.ch/record/2037702.

[33] ATLAS Collaboration, *Performance of pile-up mitigation techniques for jets in pp collisions at $\sqrt{s}$ = 8 TeV using the ATLAS detector*, Eur. Phys. J. C **76** (2016) 581, arXiv: 1510.03823 [hep-ex].

[34] ATLAS Collaboration, *Jet energy scale measurements and their systematic uncertainties in proton–proton collisions at $\sqrt{s}$ = 13 TeV with the ATLAS detector*, Phys. Rev. D **96** (2017) 072002, arXiv: 1703.09665 [hep-ex].

[35] ATLAS Collaboration, *Performance of missing transverse momentum reconstruction with the ATLAS detector using proton-proton collisions at $\sqrt{s}$ = 13 TeV*, (2018), arXiv: 1802.08168 [hep-ex].

[36] ATLAS Collaboration, *Performance of missing transverse momentum reconstruction with the ATLAS detector in the first proton–proton collisions at $\sqrt{s}$ = 13 TeV*, ATL-PHYS-PUB-2015-027, 2015, URL: https://cds.cern.ch/record/2037904.

[37] ATLAS Collaboration, *Search for new phenomena in events with a photon and missing transverse momentum in pp collisions at $\sqrt{s}$ = 13 TeV with the ATLAS detector*, JHEP **06** (2016) 059, arXiv: 1604.01306 [hep-ex].

[38] ATLAS Collaboration, *Measurement of the inclusive isolated prompt photon cross section in pp collisions at $\sqrt{s}$ = 7 TeV with the ATLAS detector*, Phys. Rev. D **83** (2011) 052005, arXiv: 1012.4389 [hep-ex].

[39] S. Dulat et al., *New parton distribution functions from a global analysis of quantum chromodynamics*, Phys. Rev. D **93** (2016) 033006, arXiv: 1506.07443 [hep-ph].

[40] L. A. Harland-Lang, A. D. Martin, P. Motylinski and R. S. Thorne, *Parton distributions in the LHC era: MMHT 2014 PDFs*, Eur. Phys. J. C **75** (2015) 204, arXiv: 1412.3989 [hep-ph].

[41] K. A. Olive et al., *Review of Particle Physics*, Chin. Phys. C **38** (2014) 090001.

[42] ATLAS Collaboration, *ATLAS Pythia 8 tunes to 7 TeV data*, ATL-PHYS-PUB-2014-021, 2014, URL: https://cds.cern.ch/record/1966419.

[43] M. Grazzini, S. Kallweit and M. Wiesemann, *Fully differential NNLO computations with MATRIX. Fully differential NNLO computations with MATRIX*, tech. rep. CERN-TH-2017-232, 2017, arXiv: 1711.06631 [hep-ph], URL: https://cds.cern.ch/record/2293309.

[44] J. M. Campbell, R. K. Ellis and C. Williams, *Vector boson pair production at the LHC*, JHEP **07** (2011) 018, arXiv: 1105.0020 [hep-ph].

[45] S. Frixione, *Isolated photons in perturbative QCD*, Phys. Lett. B **429** (1998) 369, arXiv: hep-ph/9801442.

[46] J. Butterworth et al., *PDF4LHC recommendations for LHC Run II*, J. Phys. G **43** (2016) 023001, arXiv: 1510.03865 [hep-ph].

[47] J. Campbell et al., *$Z\gamma$ production at NNLO including anomalous couplings*, JHEP **11** (2017) 150, arXiv: 1708.02925 [hep-ph].

[48] G. D'Agostini, *A Multidimensional unfolding method based on Bayes' theorem*, Nucl. Instrum. Meth. A **362** (1995) 487.

[49] U. Baur and E. Berger, *Probing the weak-boson sector in $Z\gamma$ production at hadron colliders*, Phys. Rev. D **47** (1993) 4889.

[50] A. Barroso, F. Boudjema, J. Cole, N. Dombey, *Electromagnetic properties of the Z boson. I*, Zeitschrift für Physik C **28** (1 1985) 149.

[51] C. Degrande et al., *Effective Field Theory: A Modern Approach to Anomalous Couplings*, Annals of Physics **335** (2013) 21, arXiv: 1205.4231 [hep-ph].

[52] C. Degrande, *A basis of dimension-eight operators for anomalous neutral triple gauge boson interactions*, JHEP **02** (2014) 101, arXiv: 1308.6323 [hep-ph].